

Autonomous sputter synthesis of thin film nitrides with composition controlled by Bayesian optimization of optical plasma emission

Cite as: APL Mater. 11, 071119 (2023); doi: 10.1063/5.0159406

Submitted: 23 May 2023 • Accepted: 4 July 2023 •

Published Online: 21 July 2023



View Online



Export Citation



CrossMark

Davi M. Fébba,^{a)} Kevin R. Talley, Kendal Johnson, Stephen Schaefer, Sage R. Bauers, John S. Mangum, Rebecca W. Smaha, and Andriy Zakutayev^{a)}

AFFILIATIONS

Materials Science Center, National Renewable Energy Laboratory (NREL), Golden, Colorado 80401, USA

^{a)}Authors to whom correspondence should be addressed: Andriy.Zakutayev@nrel.gov and DaviMarcelo.Febba@nrel.gov

ABSTRACT

Autonomous experimentation has emerged as an efficient approach to accelerate the pace of material discovery. Although instruments for autonomous synthesis have become popular in molecular and polymer science, solution processing of hybrid materials, and nanoparticles, examples of autonomous tools for physical vapor deposition are scarce yet important for the semiconductor industry. Here, we report the design and implementation of an autonomous workflow for sputter deposition of thin films with controlled composition, leveraging a highly automated sputtering reactor custom-controlled by Python, optical emission spectroscopy (OES), and a Bayesian optimization algorithm. We modeled film composition, measured by x-ray fluorescence, as a linear function of plasma emission lines monitored during co-sputtering from elemental Zn and Ti targets in an N₂ and Ar atmosphere. A Bayesian control algorithm, informed by OES, navigates the space of sputtering power to fabricate films with user-defined compositions by minimizing the absolute error between desired and measured optical emission signals. We validated our approach by autonomously fabricating Zn_xTi_{1-x}N_y films that deviate from the targeted cation composition by a relative $\pm 3.5\%$, even for 15 nm thin films, demonstrating that the proposed approach can reliably synthesize thin films with a specific composition and minimal human interference. Moreover, the proposed method can be extended to more difficult synthesis experiments where plasma intensity lines depend non-linearly on pressure, or the elemental sticking coefficients strongly depend on the substrate temperature.

© 2023 Author(s). All article content, except where otherwise noted, is licensed under a Creative Commons Attribution (CC BY) license (<http://creativecommons.org/licenses/by/4.0/>). <https://doi.org/10.1063/5.0159406>

08 August 2023 21:22:20

I. INTRODUCTION

Advances in robotics, machine-learning, and data science are driving progress in materials science through a data-driven approach, considered the fourth scientific paradigm¹ after experimental, theoretical, and computational approaches. With the rise of self-driving laboratories, the synthesis and characterization of materials can now be carried out with minimal human intervention and at a faster pace due to the efficient exploration of vast spaces of experimental variables by decision-making algorithms.^{2–6}

Contrary to solution-processed hybrid materials, autonomous synthesis of inorganic thin films by physical vapor deposition (PVD) is rather scarce,⁴ especially in sputtering, despite its widespread use in research and industry. Some of the few existing reports of autonomous PVD include the synthesis and optimization of

SrRuO₃^{7,8} and TiN⁹ thin films prepared by molecular beam epitaxy (MBE). A report on Nb-doped TiO₂¹⁰ thin films prepared by sputtering is so far the only work reporting a fully autonomous closed-loop PVD synthesis instrument with *in situ* measurements and feedback to a control algorithm.

Although these studies focused on the optimization of material properties such as resistivity and crystallinity, precise control of cation and anion composition in inorganic thin films is of paramount importance. For example, it has been theoretically predicted¹¹ and experimentally¹² demonstrated that short-range ordering tunes the optical absorption edge in the long-range disordered alloy (ZnSnN₂)_{1-x}(ZnO)_{2x} at a very specific composition of $x = 0.25$. In addition, the resistivity and bandgap of ternary nitrides and their alloys depend mostly on cation composition.^{13,14} Furthermore, many promising oxynitrides were recently predicted to

possess semiconductor electrical transport and ferroelectric polarization properties similar to halide perovskites but with longer-term stability.¹⁵ However, the specific O:N = 2:1 ratio required for these properties is challenging to control during synthesis.¹⁶

In this context, we report the design and implementation of an autonomous instrument for controlling the composition of thin films with minimal human intervention, leveraging a highly automated sputtering reactor and optical emission spectroscopy (OES). By fabricating $Zn_xTi_{1-x}Ny$ thin films with simultaneous monitoring of optical emission lines from the sputtering of elemental targets, we show that cation composition, spanning a wide range, can be expressed as a function of plasma emission lines only.

Informed by OES measurements, a closed-loop control algorithm with Bayesian optimization as its decision-making agent can effectively optimize the power on each sputtering source to fabricate thin films with a specific cation composition defined prior to deposition with minimal human interference. Moreover, we show that our model can accurately predict film composition regardless of total power or gas flow as long as the OES signal is reproduced, but re-calibration is needed if autonomous depositions are carried out at chamber pressures different from those set during model calibration.

II. OVERVIEW OF THE SPUTTERING INSTRUMENT

To enable the autonomous synthesis of thin films with controlled composition, we recently designed and built a highly-automated sputtering reactor. Equipped with four sputtering sources (cathodes) and able to source bias to the substrate, this high-vacuum ($< 1 \times 10^{-7}$ Torr) instrument allows the exploration of a wide substrate temperature range, from cryogenic temperatures up to 1000°C .

Figure 1 shows a high-level diagram of this system, depicting sputtering sources, the distribution of process gases, and data flow. Additional capabilities include control of gas mixing and distribution to key locations within the sputtering environment (such as individual targets and the substrate), time-sequenced shutters, and pressure control via positioning of the gate valve to the turbo molecular pump.

The high degree of automation of this sputtering instrument was accomplished by connecting all its sensors and actuators, such as pressure gauges, power supplies, and pneumatic valves, to a Graphite Edge controller (Red Lion Controls) that interfaces with the user through a Human-Machine Interface (HMI), developed with Crimson 3.1.

This approach allows the implementation of customized software solutions and enables the user to execute complex programmable synthesis recipes, besides offering room for further custom automation. Moreover, real-time deposition data of sputtering parameters (such as power, voltage, pressure, and gas flow) are recorded and loaded into a data warehouse.¹⁷

A unique feature of this reactor is that the Graphite Edge controller supports the Open Platform Communications Unified Architecture protocol (OPC UA), acting as a server. In this way, a Python client can directly communicate with the controller through the Python OPC UA libraries, effectively controlling all chamber parameters.

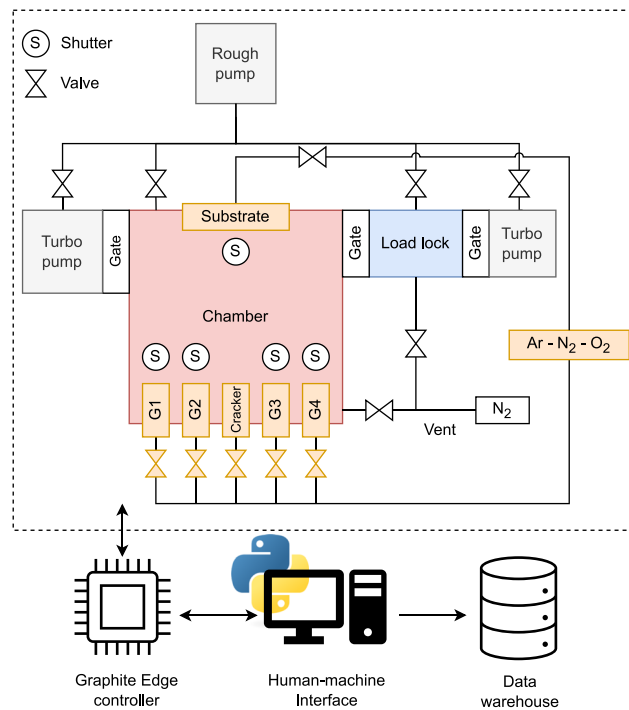


FIG. 1. Diagram of the autonomous sputtering system, showing gas distribution, sputtering sources, and data flow. A Python script controls all chamber parameters by interacting with a Graphite Edge controller, and real-time deposition data are recorded and stored in a data warehouse.

Therefore, Python libraries for machine learning and optimization can be leveraged to control sputtering parameters in real-time, which is usually not possible for chambers and accompanying systems available, making this instrument an excellent platform for implementing an autonomous workflow for the synthesis of thin films.

III. OPTICAL EMISSION SPECTROSCOPY

Optical emission spectroscopy (OES) is a passive optical diagnostic method that analyzes light emitted from excited atoms and molecules in a plasma environment. Due to its simplicity and non-intrusive aspect, it was one of the earliest techniques applied to the analysis of sputtering plasma.¹⁸

The basic physical process in OES is the excitation of particles by electron impact from level i to level j and decay into level k by spontaneous emission with transition probability A_{jk} , resulting in a line emission ε_{jk} with wavelength $\lambda = hc/(E_j - E_k)$, where h is the Planck's constant, c is the speed of light, and E_j and E_k are the energy levels of states j and k , respectively.

This wavelength is detected by the emission spectrometer and is a fingerprint for the radiating particle,¹⁹ while line intensities are proportional to the density of particles in the plasma.²⁰ It has been shown by previous studies that the intensity of emission lines monitoring during sputtering can be connected to the resulting film composition^{21,22} and material properties,²³⁻²⁵ besides being useful for process control.^{26,27}

In glow discharge optical emission spectroscopy (GDOES), a sample of interest acts as a cathode and is sputtered, usually with Ar. By analyzing the emitted light with a spectrometer, the elemental composition of the sample and depth profile analysis can be carried out since the basic assumption is that the intensity of a certain emission line of an element is a function of the concentration of this element in the analyzed material.²⁸

Since it is a comparative technique, it needs calibration:²⁹ reference materials of known composition must be analyzed in order to build a calibration function $I_{\lambda(X),M} = f(c_{E,M})$, where X is the element to be detected in the material M and $I_{\lambda(X)}$ is the line intensity at wavelength λ of the element X with concentration c in the material M .

IV. CALIBRATION

Optical emission spectroscopy can measure film composition after a calibration procedure is performed, which consists of finding a relation between the intensity of emission lines of interest and film composition, which must be measured by a direct technique. In this section, we will discuss each part of this procedure: fabrication of thin films and composition measurement by energy dispersive X-ray fluorescence (EDXRF), OES characterization, and establishing a connection between EDXRF and OES measurements through an analytical function.

A. Thin film fabrication

To demonstrate autonomous synthesis of thin films with controlled composition, $Zn_xTi_{1-x}N_y$ was considered a validation case as it has been successfully synthesized by our group¹³ in the sputtering instrument described in Sec. II. In this work, we assume nitrogen composition will fall on the $TiN-ZnTiN_2-Zn_3N_2$ tie lines, although it is not explicitly measured since the cation composition is our focus.

We fabricated thin films on glass substrates (2×2 in.² Corning Eagle XG Glass). Before each deposition, the chamber was evacuated at pressures lower than 1×10^{-7} Torr after transferring the substrate from a load lock chamber. Two-inch diameter Zn (99.99% purity) and Ti (99.995% purity) elemental targets were excited by radio-frequency (RF) sputtering sources. Common to all depositions, the chamber pressure was set at 10 mTorr after introducing 20 sccm of Ar adjacent to each sputtering source (40 sccm total) and 20 sccm of N₂ adjacent to the substrate gas inlet.

Depositions lasted between 45–120 min, always after a pre-sputtering step of 30 min with the substrate shutter closed to clean the surface of the targets, and no substrate heating or cooling was applied. The substrate was rotated during deposition to grow films with a homogeneous composition. Figure 2(a) shows a sample of zinc titanium nitride fabricated by this process.

Several depositions were carried out with varying powers applied to each target. The resulting films spanned a wide composition, expressed as the average of $Zn/(Zn + Ti)$ (at. %) in Fig. 2(b), obtained by EDXRF measurements taken at 44 distinct spots on the film [Fig. 2(a)] with a Fischerscope X-ray XDV EDXRF instrument and accompanying WinFTM analysis software. The average thickness, estimated from EDXRF (calibrated with ellipsometry measurements¹³), was between (18.0 ± 0.2) nm and (110.0 ± 0.3) nm for all

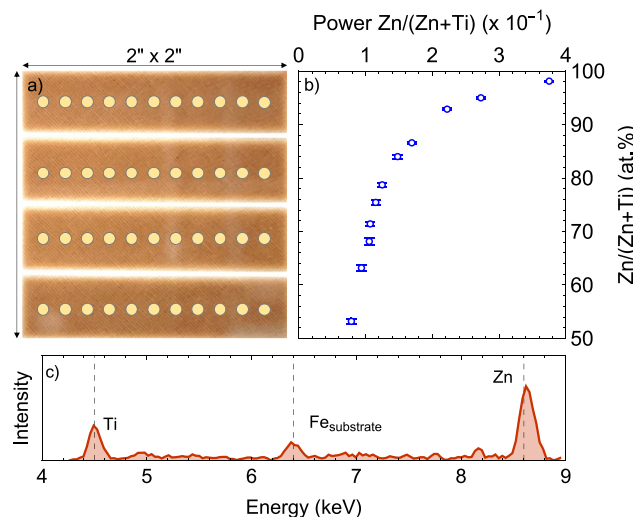


FIG. 2. (a) Picture of a sample fabricated on a 2×2 in.² glass substrate, with approximate positions of EDXRF measurements. Diagonal striations are from a cotton cloth underneath the substrate. (b) Average cation composition as a function of power ratio on Zn and Ti targets, obtained from EDXRF measurements across 44 points on the film. (c) Example of an EDXRF spectrum measured at a single spot, showing Zn and Ti K α spectral lines used for composition analysis and a Fe line from the substrate.

depositions. Uncertainty in composition and thickness was taken as two times the standard uncertainty, i.e., $2s/\sqrt{n}$, where s is the standard deviation of 44 measurements (n), resulting in a confidence interval (C.I.) of $\sim 95\%$.

The range of power applied to each sputtering source takes into account the maximum power allowed on each 2 in target as well as the minimum required to sustain a plasma. Therefore, powers ranging from 12 to 30 W and 50 to 140 W for the Zn and Ti targets, respectively, resulted in samples with an average composition spanning the range 53%–98%, as summarized in Fig. 2. Although it could be possible to obtain cation compositions below 50% Zn/(Zn + Ti) (at. %), the power on the Zn target would be too small, below 12 W, which would seem to result in films with irreproducible composition for the same chamber conditions. On the other hand, the power on the Ti target would be at a maximum of 150 W and could not be increased without risking damage to the target.

B. Plasma monitoring

To enable in-vacuum plasma monitoring with OES in our sputtering system, 2 in. stainless steel chimneys were specially adapted to accommodate 90° collimators with a 3° acceptance angle, as shown in Fig. 3(a), each monitoring the glow discharge just above the target.

During each deposition, optical emission spectra from each target were independently recorded by a multi-channel Plasus Emicon MC spectrometer between 195 and 1105 nm, avoiding signal interference during co-sputtering. A useful feature of this setup is that each collimator is equipped with a coating-protection device consisting of a quartz plate and a capillary cartridge to avoid deposition of sputtered material on the collimator optics.

Each spectrometer integration time was set to 50 ms, and 10 spectra were collected and averaged to increase the signal-to-noise

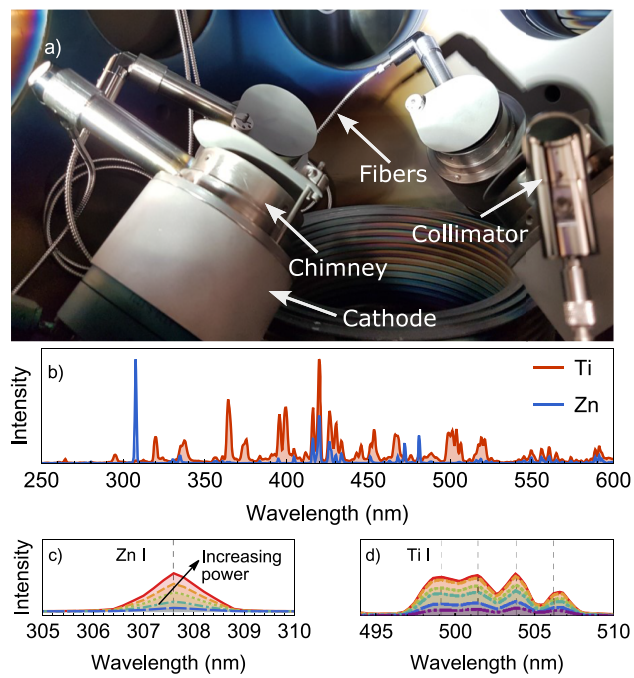


FIG. 3. (a) Internal view of the process chamber, showing 2 in. chimneys adapted to accommodate 90° collimators to collect emission spectra from each sputtering source. (b) Optical emission spectra from Zn and Ti targets sputtered with Ar between 250 and 600 nm, where most of the Ti I and Zn I lines are found. Increase of Zn I (c) and Ti I (d) emission lines for increasing sputtering power on each target.

ratio, amounting to a total recording time of about 500 ms per spectrum. Background OES spectra were collected before igniting the plasma on the sputtering sources and then subtracted from all subsequent measurements.

Spectrum measurement and signal processing were carried out with the Plasus Emicon MC software that accompanies the spectrometer, while analysis of emission lines was accomplished with the Specline software, which has an extensive database of spectral lines for atoms, ions, and molecules and features automated line detection based on the elements of interest.

To detect non-overlapping Ti and Zn lines that are sensitive to changes in sputtering power, the Ti and Zn targets were initially sputtered with Ar at 10 mTorr by injecting 20 sccm of Ar through a gas inlet adjacent to each sputtering source. Figure 3(b) shows that a Zn I line at 307.5 nm and Ti I lines between 496 and 510 nm are suitable choices since they do not show any overlap and are intense enough to be detected with the aforementioned spectrometer acquisition settings.

Moreover, these lines are also sensitive to changes in power, as shown in Figs. 3(c) and 3(d). However, to avoid inaccurate signal evaluation due to broadening and peak shift, common in OES analysis,³⁰ the integral under the emission signal was taken instead of line intensities. For simplicity, we will refer to this integral as intensity only.

Therefore, to incorporate information from both sputtering targets into the analysis, the normalized ratio was taken, as given by the following equation Eq. (1)

$$I_{OES} = \frac{I_{Zn}}{I_{Zn} + I_{Ti}}, \quad I_{Zn} = \int_{306}^{310} I d\lambda, \quad I_{Ti} = \int_{496}^{510} I d\lambda, \quad (1)$$

where I is the intensity of the optical emission signal monitored by independent channels over each target. Then, considering that I_{OES} was observed to be stable over time, the median of I_{OES} was taken between signal stabilization—10 min from plasma ignition—and the end of deposition, so that a single OES parameter characterizes the plasma environment.

C. Analytical function

In GDOES, the goal is initially to find a calibration function: a model that describes emission lines as a function of elemental composition in reference samples of known composition.²⁹ Then, to characterize samples of unknown composition, this calibration function is mathematically inverted, and the resulting model is called the analytical function. By measuring the intensity of a specific line of element X , its composition in a material M can be obtained.³¹

Therefore, in our approach, we establish an analytical function through the calibration procedure, i.e., fabricating samples and measuring their composition with EDXRF, and then finding a model to express film composition as a function of the normalized ratio of intensity of emission lines given by Eq. (1). Figure 4 shows that a simple linear relation between I_{OES} and composition was obtained, with $R^2 = 0.995$, a root mean square error of 1.0×10^{-2} , and a maximum residual of 2.1 percentage points.

All depositions and OES measurements taken to find this analytical function were carried out on different days, spanning several weeks, including many sources of random changes, such as venting the chamber to perform routine maintenance work, inspection of the collimators for possible coating, and so on. Therefore, the analytical function incorporates all these changes that occurred over time, making the model more robust against these sources of noise. However, for future experiments, all the steps for the calibration procedure can be completed in about one day to avoid these sources of noise.

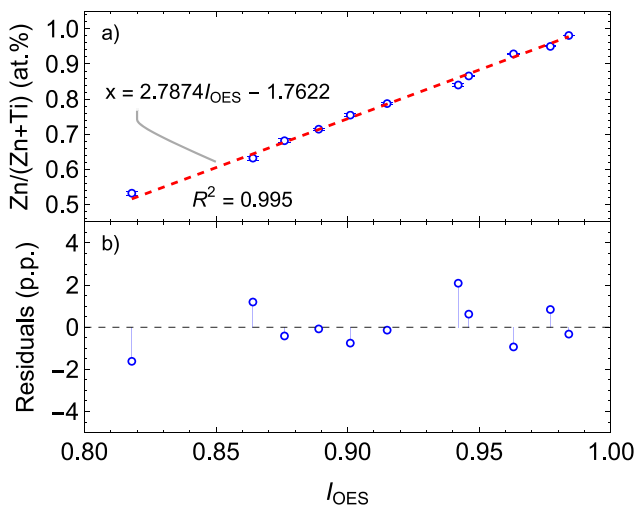


FIG. 4. Linear fit of $Zn/(Zn + Ti)$ (at.%) in $Zn_xTi_{1-x}N_y$ as a function of OES signal (a) and corresponding residuals (b), expressed as percentage points (p.p.).

V. CONTROL ALGORITHM

An autonomous closed-loop control system leveraging the high degree of automation of our sputtering reactor was implemented using Python. The flowchart in Fig. 5 summarizes the workflow. At its core, a Bayesian optimization algorithm, implemented with the scikit-optimize (*skopt*)³² package, controls the radio frequency sputtering power on elemental targets (Zn and Ti, in this study) and, informed by OES measurements, explores the 2D-space of power applied on the targets until a user-defined OES signal (I_{OES}) that corresponds to a specific film composition is obtained.

The goal of the optimization algorithm is to minimize an objective function, which in this case is the absolute error between the measured I_{OES} and the user-defined I_{OES} (setpoint), given by the following equation:

$$\text{objective} = |I_{OES}^{\text{current}} - I_{OES}^{\text{setpoint}}|, \quad (2)$$

where $I_{OES}^{\text{current}} = \text{median}(I_{OES})$ over the last 10 s of data to filter out measurement noise.

A Gaussian process was employed as a surrogate model for the unknown function that models Eq. (2) as a function of the sputtering powers on the targets. The Radial Basis Function (squared-exponential) was used as the kernel, with its hyperparameters optimized at each optimization loop by scikit.

After loading the substrate into the chamber, the only step requiring human intervention is to define start-up optimization and chamber parameters, such as process pressure, gas flows, and power on each target, and to specify the desired OES signal (setpoint).

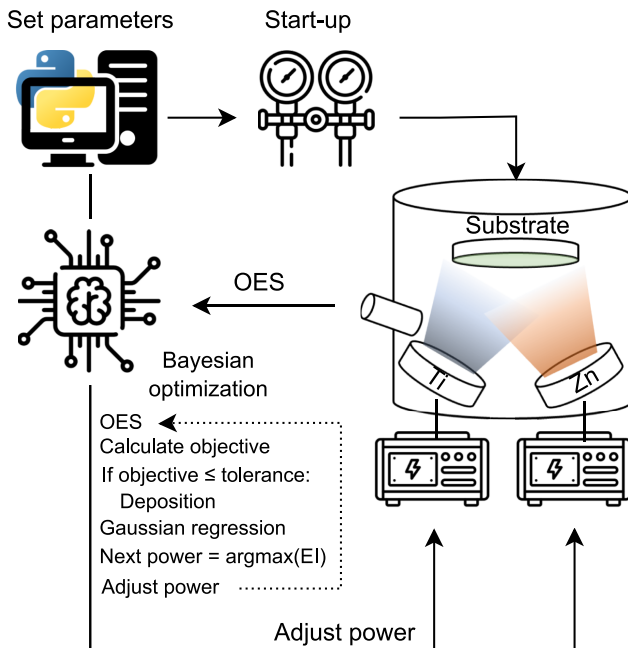


FIG. 5. Flowchart of the autonomous sputtering workflow. After automatic chamber start-up, a Bayesian optimization algorithm controls the sputtering powers based on the analysis of optical emission signals from each target. The only step requiring human intervention is to set up the initial chamber and optimization parameters.

Upon setting these initial parameters, the control algorithm initially checks for high vacuum conditions in the sputtering chamber. If this condition is satisfied, an automatic routine ignites the plasma on each sputtering source, adds reactive gas (N_2) through the substrate gas inlet, and controls the chamber pressure.

A countdown for OES signal stabilization begins, and after it completes, the Bayesian optimization loop starts. Starting with an arbitrary pair of sputtering powers on the two targets set during start-up, the optimization algorithm checks if I_{OES} is stable by verifying it is within a maximum allowed deviation of 3 % from its median over the last 10 s of data. Then, if the signal is stable, it measures I_{OES}^{current} and calculates the objective function given by Eq. (2).

If the objective is higher than a tolerance criterion, a Gaussian process is then fitted to the data, and the point where the Expected Improvement (EI) acquisition function is maximized is then suggested as the next sampling point within a search space. A new pair of sputtering powers is then set on the RF power supplies connected to the sputtering sources and adjusted by a ramp procedure at a rate of 2 W s^{-1} (user-defined) to avoid plasma destabilization due to fast changes in power.

The algorithm then waits for signal stabilization and takes another I_{OES}^{current} measurement. This whole process—OES analysis, evaluation of the objective function, Gaussian regression, sampling the next point—continues until convergence is achieved (i.e., the objective function falls below a tolerance criterion) or a maximum number of iterations is reached, as depicted in Fig. 5. If the convergence criterion is satisfied, the substrate shutter is automatically opened, and deposition starts.

Although the sputtering powers could be controlled by a more conventional Proportional-Integral-Derivative (PID) approach³³ to minimize the objective function, human tuning of PID parameters to control the growth variables represents a serious bottleneck for an autonomous framework, especially if more variables must be controlled, hindering scalability and maintainability since the re-tuning of these parameters is often needed. Conversely, a control method based on Bayesian optimization eliminates these issues by efficiently sampling the search space and refining the surrogate model in a data-driven approach. Our knowledge about the likely objective function improves as more data are observed.³⁴

Note that this optimization problem is a degenerate one: several sets of power levels can lead to the same OES signal. As we will discuss later in Sec. VI B, our approach of taking the first set of powers for which the algorithm finds convergence does not lead to any detriment in the prediction results since, as long as the desired OES signal is obtained, the composition will not significantly change.

VI. RESULTS

A. Validation

To validate the proposed approach, the aim was to fabricate films with a specific composition, defined prior to deposition: 75%, 95%, 65%, and 85% Zn/(Zn + Ti) (at. %), denoted as validation runs 1, 2, 3, and 4, respectively, in Table I. Zn-rich conditions were chosen due to irreproducible OES measurements and film composition obtained at low powers on the Zn target, as previously mentioned,

TABLE I. Results of the validation experiments, with relative errors between predicted and actual film composition, expressed as Zn/(Zn + Ti) (at. %) and averaged across 44 distinct spots on the substrate.

Run	Goal (%)	Predicted (%)	Actual (%)	Prediction error (%)
1	75	75.0	76.9 ± 0.4	-2.5
2	95	95.3	92.2 ± 0.1	3.4
3	65	64.6	65.5 ± 0.3	-1.4
4	85	85.3	86.3 ± 0.6	-1.2

and the search range for the Bayesian algorithm was set as 50–150 W for the Ti target and 13–45 W for the Zn target.

For these experiments, the sputtering chamber was kept at 10 mTorr by adding 20 sccm of Ar through each sputtering source and 20 sccm of N₂ through the substrate, as in the calibration procedure. We then set 10 min as the initial stabilization window after automatic plasma ignition, which was reduced to 2 min after ramping the power on the sputtering sources during the optimization loop.

After chamber start-up with arbitrary sputtering powers, the control system adjusts the powers to obtain OES signals that would result in films with the desired composition. The algorithm was allowed to run for up to 30 iterations, and the convergence threshold was set as 6×10^{-3} , which was found to guarantee convergence and resulted in a good trade-off between convergence time and accuracy of the predicted film composition.

Figure 6(a) shows the evolution of the emission signal as a function of time while the Bayesian optimization algorithm searches for the best set of powers to achieve the desired setpoint signal. After

convergence is achieved, the OES signal is stable over time until the deposition ends.

Although convergence was fast for Runs 1 and 2, as shown in Fig. 6(b), with only 5 and 3 iterations needed for convergence, respectively, the algorithm sometimes needs more iterations due to its stochastic nature, as seen for Run 3, which took 17 iterations. Nonetheless, the algorithm was able to achieve convergence for all four validation runs. Moreover, Figs. 6(c)–6(f) show the values of sputtering powers explored by the Bayesian optimization algorithm and the resulting objective function for all the validation runs.

To verify whether the resulting films had the targeted compositions, EDXRF measurements were carried out across 44 spots on the substrate, and the average value was taken as the film composition, as previously discussed. Since the algorithm had a convergence threshold for the OES signal taken as the optimum (convergence happens when $objective \leq 6 \times 10^{-3}$), we report the predicted composition, i.e., the composition predicted from the analytical function from Fig. 4 based on the OES measurement taken at the last iteration of the optimization routine. The average film thickness was (26.7±0.2) nm, (141.6±0.4) nm, (41.6±0.3) nm, and (15.4±0.2) nm for samples 1, 2, 3, and 4, respectively.

Prediction errors, calculated as $(predicted/actual - 1)$, express the relative error between predicted and actual film composition. As shown in Table I, the proposed approach was able to autonomously fabricate thin films with compositions within 3.5 % of the desired value. As more depositions are carried out with simultaneous plasma monitoring, the resulting OES signal and film composition can be retrofitted into the analytical function to improve its accuracy in predicting film composition. Other routes of improvement include the fabrication of thicker films for higher precision EDXRF

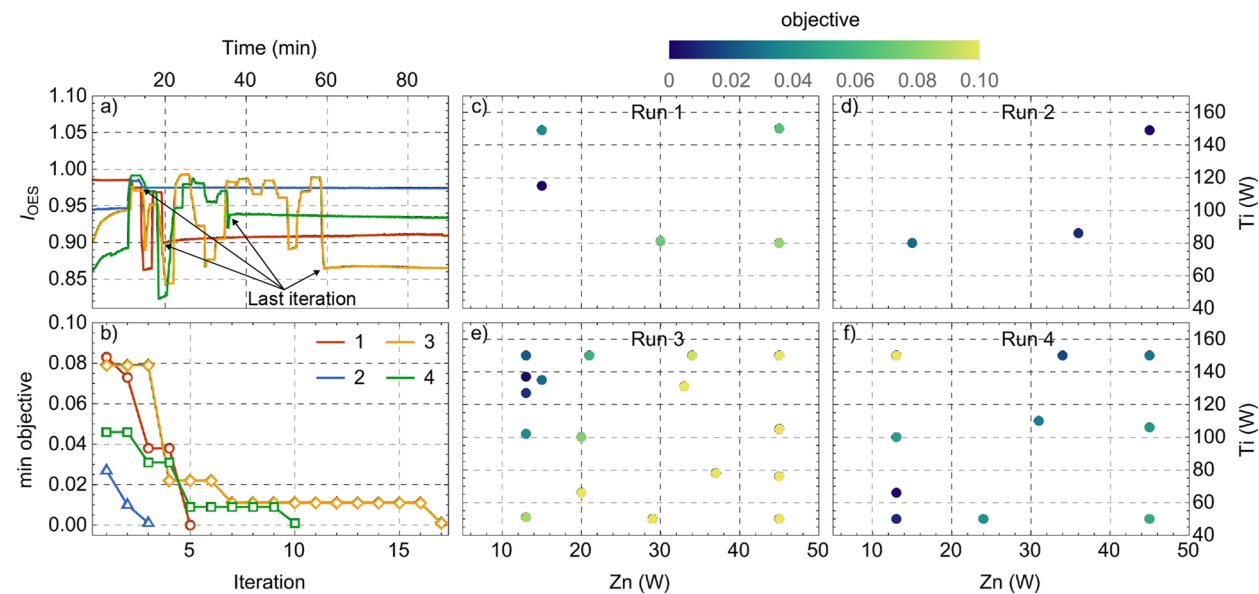


FIG. 6. Optimization results for four validation runs. OES signal as a function of time (a), while the Bayesian optimization algorithm searches for the optimal sputtering powers. The convergence plot (b) shows the evolution of the minimum of the objective function, while (c)–(f) show the sputtering powers visited by the algorithm for each validation run, with colors representing the value of the objective function.

measurements, waiting a longer time for OES signal stabilization after a new power set is suggested by the algorithm, and reducing the convergence criterion from 6×10^{-3} , at the expense of convergence time.

B. Degeneracy: Total power effects

We studied if degeneracy would have any adverse effects on the prediction results. As previously mentioned, the optimization problem of finding the optimal set of sputtering powers to achieve a desired OES signal is a degenerate one: several sets of powers may result in the same signal.

For this study, we varied the power applied to each target for three independent depositions while keeping $I_{OES} \approx 0.902$ [dashed line on Fig. 7(a)], which corresponds to 75% Zn/(Zn + Ti) (at. %) [dashed line on Fig. 7(b)] according to the analytical function. The chamber pressure was set at 10 mTorr by adding 20 sccm of Ar through gas inlets adjacent to each sputtering source (total of 40 sccm) and 20 sccm of N₂ adjacent to the substrate, as summarized in Table II (samples 1, 2, and 3). Figure 7(a) shows that it was possible to reproduce the desired OES signal for three different sets of power levels, with a maximum deviation of 3.3×10^{-3} between the desired I_{OES} and the median of I_{OES} taken from 10 min to the end of the deposition. As seen in Fig. 7(b), the film composition did not show any significant changes, even though the powers on both targets changed. Prediction errors between actual and predicted composition (given by the analytical function from Fig. 4 based on the median of the OES signal between 10 min and the end of each deposition) were -3.8%, 1.7%, and -3.3%, respectively.

Therefore, this degeneracy caused by simultaneously optimizing two power supplies does not constitute an issue as long as the OES signal can be reproduced since the prediction errors are of the same order as those found for the validation experiments shown in Table I. However, other film properties may change, such as morphology and crystallinity, but since we are only optimizing for composition, these side effects are out of scope here.

TABLE II. Different total powers and gas flows of Ar and N₂ do not cause large relative errors when predicting film composition based on emission signals, contrary to changes in the chamber pressure, which invalidate the analytical function obtained during calibration.

Sample	Zn (W)	Ti (W)	Ar (sccm)	N ₂ (sccm)	mTorr	Error (%)
1	15	115	40	20	10	-3.8
2	17	145	40	20	10	1.7
3	13	101	40	20	10	-3.3
4	15	115	30	10	10	-2.9
5	15	115	20	15	10	-0.4
6	15	115	40	20	5	-30.0
7	15	115	40	20	15	11.7

C. Effects of chamber pressure and gas flow

We also investigated the effects of chamber pressure and gas flow on the OES signal and the accuracy of the analytical function (Fig. 4) for predicting film composition. For this purpose, we fabricated films at different total flows of Ar and N₂ and at lower (5 mTorr) and higher pressures (15 mTorr), as summarized in Table II, while keeping constant the set of sputtering powers that the algorithm found in the validation experiments for a film with 75% Zn/(Zn + Ti) (at. %): 115 and 15 W on the Ti and Zn targets, respectively.

As shown in Fig. 7(a)—samples 1, 4, and 5—the optical emission signal I_{OES} did not show significant changes for different gas flows with a constant pressure set at 10 mTorr. For these samples, predicting film composition by feeding I_{OES} into the analytical function (Fig. 4) results in small prediction errors, expressed as the relative error between actual and predicted composition, as demonstrated in Table II.

Therefore, the proposed approach can still produce reliable results for different gas flows, but only if the chamber pressure is equal to that set during the calibration step; decreasing the pressure to 5 mTorr resulted in a significant drop in the emission signal with an uncorrelated increase of Zn in the film [Fig. 7(b)—sample 6].

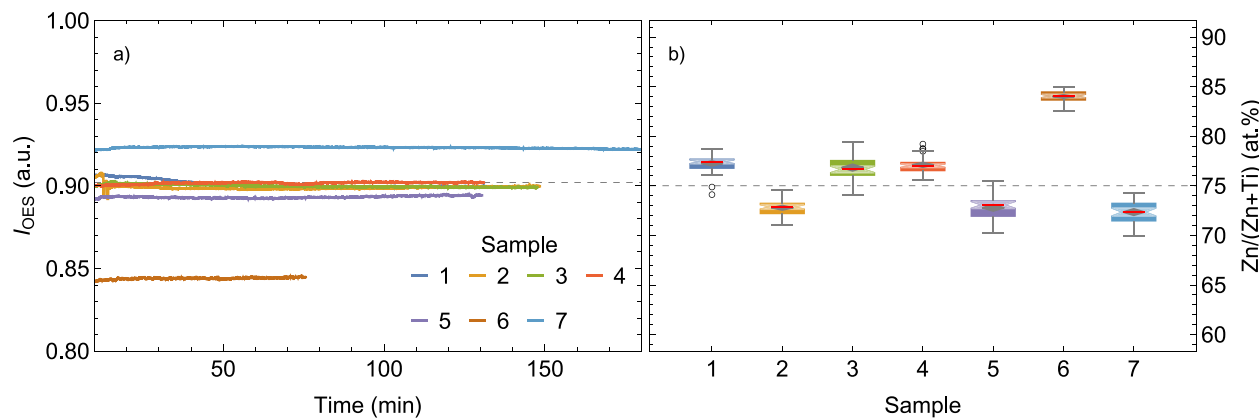


FIG. 7. Effects of total power (samples 1, 2, and 3), gas flow (samples 1, 4, and 5), and pressure (samples 6 and 7) on the OES signal (a) and film composition measured by EDXRF (b). Diamond edges and notches denote the 95% C.I. for the mean (center of gray diamonds) and median (red dash) in the notched box plots, respectively.

If the analytical function were still valid for this case, 58.8% Zn/(Zn + Ti) would be observed in the film, according to the observed emission signal. Figure 7(b) shows that the composition of Zn/(Zn + Ti) in the resulting film was 84%, thus invalidating the analytical function for depositions at pressures lower than that of the calibration procedure.

If this were an autonomous deposition with a desired 75% of Zn/(Zn + Ti) in the film, the algorithm would try to converge to the setpoint signal of 0.902 by increasing the power on Zn, decreasing the power on Ti or both, leading to an even higher percentage of Zn in the film, although the desired OES signal would be achieved.

Higher pressures lead to the same effect: increasing the pressure to 15 mTorr resulted in a shift of the emission signal toward a higher value (Fig. 7—sample 7), with an uncorrelated decrease in Zn/(Zn + Ti) (at.%) in the film to 72.4%. Although a higher pressure did not cause significant changes in actual composition, the predicted composition from the analytical function in Fig. 4 was 80.9%, resulting in a relative error close to 12%, too large for the purpose of controlling film composition. Again, if this were an autonomous deposition, the algorithm would try to reduce the emission signal, which would lead to even higher prediction errors.

VII. DISCUSSION

The effects of chamber pressure on the resulting film composition and OES signal (Fig. 7) can be explained by two effects:²⁰ at low pressures, the mean free path of the sputtered atoms increases since they do not experience a significant amount of collisions with Ar atoms and do not accumulate in the discharge, reducing the intensity of the emission signal.

On the other hand, the substrate is also sputtered by energetic particles, and lighter atoms (Ti, in this case) are preferentially resputtered from the film, which explains the higher Zn/(Zn + Ti) ratio in the film fabricated at low pressure, even though gas flows and powers were the same as for sample 1. In contrast, this phenomenon is reduced at higher pressures, explaining the decreased Zn/(Zn + Ti) ratio at 15 mTorr.

Any effects at the substrate are thus not taken into account, and substrate temperature can also cause large errors in the prediction results since the substrate heating can result in different film compositions even though the plasma conditions are the same. In this way, the variation caused by substrate effects constitutes a hindrance since several film compositions could be obtained for the same OES signal, contrary to the previously discussed degeneracy caused by total power.

Nonetheless, the proposed approach is useful for the autonomous synthesis of thin films with user-defined compositions. Taking advantage of a short calibration procedure and an automated deposition setup, several analytical functions can be quickly obtained for different pressures and substrate temperatures, making it possible to explore chamber conditions for which film quality is enhanced.

Finally, to further improve the acceleration provided by the synthesis of thin films with controlled composition, future work will focus on developing calibration procedures that are independent of chamber conditions and geometry.

VIII. CONCLUSION

We report the design and implementation of an autonomous instrument for sputter synthesis of thin films with controlled cation composition in a highly automated reactor that interfaces with Python scripts. After a calibration procedure to correlate actual film composition, measured by ex-situ energy dispersive X-ray fluorescence (EDXRF) and *in situ* optical emission spectroscopy (OES) data obtained during the RF sputtering of elemental targets, we showed that a linear function can predict composition based solely on plasma emission lines.

Informed by real-time OES measurements, a Bayesian optimization algorithm optimized the RF power applied to sputtering sources to synthesize films with a user-defined composition. As a case study, our instrument fabricated Zn_xTi_{1-x}N_y thin films targeting $x = 0.65, 0.75, 0.85$, and 0.95 . EDXRF measurements showed that the proposed approach resulted in films with $x = 0.65, 0.77, 0.86$, and 0.92 , thus in good agreement with the targeted composition.

However, for accurate results, it is crucial to maintain the chamber pressure at the level set during calibration, as any variations in this parameter can shift the optical emission signal with uncorrelated changes in the final film composition, leading to substantial inaccuracies. Conversely, changes in relative gas flows and total sputtering power do not seem to increase the prediction errors if the chamber pressure can be kept at a constant level.

ACKNOWLEDGMENTS

This work was authored by the National Renewable Energy Laboratory, operated by Alliance for Sustainable Energy, LLC, for the U.S. Department of Energy (DOE) under Contract No. DE-AC36-08GO28308. Funding is provided by the National Renewable Energy Laboratory (NREL) under the Laboratory Directed Research and Development (LDRD) program. R.W.S. acknowledges support from the Director's Fellowship within the NREL LDRD program. The views expressed in the article do not necessarily represent the views of the DOE or the U.S. Government. Schematics were designed using icons made by FreePik and VectorIcons from www.flaticon.com.

AUTHOR DECLARATIONS

Conflict of Interest

The authors have no conflicts to disclose.

Author Contributions

Davi M. Febba: Conceptualization (equal); Data curation (equal); Formal analysis (equal); Investigation (equal); Methodology (equal); Software (equal); Validation (equal); Visualization (equal); Writing – original draft (equal); Writing – review & editing (equal). **Kevin R. Talley:** Resources (supporting). **Kendal Johnson:** Methodology (supporting); Resources (supporting); Software (supporting); Writing – review & editing (equal). **Stephen Schaefer:** Resources (supporting); Writing – review & editing (equal). **Sage R. Bauers:** Writing – review & editing (equal). **John S. Mangum:** Writing –

review & editing (equal). **Rebecca W. Smaha:** Writing – review & editing (equal). **Andriy Zakutayev:** Conceptualization (equal); Data curation (equal); Formal analysis (equal); Funding acquisition (equal); Investigation (equal); Methodology (equal); Project administration (equal); Resources (equal); Software (equal); Supervision (equal); Validation (equal); Visualization (equal); Writing – original draft (equal); Writing – review & editing (equal).

DATA AVAILABILITY

The data that support the findings of this study are available from the corresponding authors upon reasonable request.

REFERENCES

- ¹L. Himanen, A. Geurts, A. S. Foster, and P. Rinke, “Data-driven materials science: Status, challenges, and perspectives,” *Adv. Sci.* **6**, 1900808 (2019).
- ²M. Abolhasani and E. Kumacheva, “The rise of self-driving labs in chemical and materials sciences,” *Nat. Synth.* **2**, 483–492 (2023).
- ³J. H. Montoya, M. Aykol, A. Anapolksky, C. B. Gopal, P. K. Herring, J. S. Hummelshøj, L. Hung, H.-K. Kwon, D. Schweigert, S. Sun, S. K. Suram, S. B. Torrisi, A. Trewartha, and B. D. Storey, “Toward autonomous materials research: Recent progress and future challenges,” *Appl. Phys. Rev.* **9**, 011405 (2022).
- ⁴N. J. Szymanski, Y. Zeng, H. Huo, C. J. Bartel, H. Kim, and G. Ceder, “Toward autonomous design and synthesis of novel inorganic materials,” *Mater. Horiz.* **8**, 2169–2198 (2021).
- ⁵E. Stach, B. DeCost, A. G. Kusne, J. Hattrick-Simpers, K. A. Brown, K. G. Reyes, J. Schrier, S. Billinge, T. Buonassisi, I. Foster, C. P. Gomes, J. M. Gregoire, A. Mehta, J. Montoya, E. Olivetti, C. Park, E. Rotenberg, S. K. Saikin, S. Smullin, V. Staney, and B. Maruyama, “Autonomous experimentation systems for materials development: A community perspective,” *Matter* **4**, 2702–2726 (2021).
- ⁶H. S. Stein and J. M. Gregoire, “Progress and prospects for accelerating materials science with automated and autonomous workflows,” *Chem. Sci.* **10**, 9640–9649 (2019).
- ⁷Y. K. Wakabayashi, T. Otsuka, Y. Krockenberger, H. Sawada, Y. Taniyasu, and H. Yamamoto, “Machine-learning-assisted thin-film growth: Bayesian optimization in molecular beam epitaxy of SrRuO₃ thin films,” *APL Mater.* **7**, 101114 (2019).
- ⁸Y. K. Wakabayashi, T. Otsuka, Y. Krockenberger, H. Sawada, Y. Taniyasu, and H. Yamamoto, “Bayesian optimization with experimental failure for high-throughput materials growth,” *Npj Comput. Mater.* **8**, 180 (2022).
- ⁹I. Ohkubo, Z. Hou, J. N. Lee, T. Aizawa, M. Lippmaa, T. Chikyow, K. Tsuda, and T. Mori, “Realization of closed-loop optimization of epitaxial titanium nitride thin-film growth via machine learning,” *Mater. Today Phys.* **16**, 100296 (2021).
- ¹⁰R. Shimizu, S. Kobayashi, Y. Watanabe, Y. Ando, and T. Hitosugi, “Autonomous materials synthesis by machine learning and robotics,” *APL Mater.* **8**, 111110 (2020).
- ¹¹J. Pan, J. J. Cordell, G. J. Tucker, A. Zakutayev, A. C. Tamboli, and S. Lany, “Perfect short-range ordered alloy with line-compound-like properties in the ZnSnN₂:ZnO system,” *Npj Comput. Mater.* **6**, 63 (2020).
- ¹²C. L. Melamed, M. K. Miller, J. Cordell, L. Pucurimay, A. Livingood, R. R. Schepf, J. Pan, K. N. Heinselman, F. D. Vila, A. Mis, D. Nordlund, B. Levy-Wendt, S. Lany, E. S. Toberer, S. T. Christensen, and A. C. Tamboli, “Short-range order tunes optical properties in long-range disordered ZnSnN₂–ZnO alloy,” *Chem. Mater.* **34**, 3910–3919 (2022).
- ¹³A. L. Greenaway, S. Ke, T. Culman, K. R. Talley, J. S. Mangum, K. N. Heinselman, R. S. Kingsbury, R. W. Smaha, M. K. Gish, E. M. Miller, K. A. Persson, J. M. Gregoire, S. R. Bauers, J. B. Neaton, A. C. Tamboli, and A. Zakutayev, “Zinc titanium nitride semiconductor toward durable photoelectrochemical applications,” *J. Am. Chem. Soc.* **144**, 13673–13687 (2022).
- ¹⁴D. Fébba, V. Paratte, L. Antognini, J. Dréon, J. Hurni, J. Thomet, R. Rubinger, E. Bortoni, C. Ballif, and M. Boccard, “Effects of work function and electron affinity on the performance of carrier-selective contacts in silicon solar cells using ZnSn_xGe_{1-x}N₂ as a case study,” *IEEE J. Photovoltaics* **11**, 1350–1357 (2021).
- ¹⁵S. T. Hartman, A. S. Thind, and R. Mishra, “Tin oxynitride-based ferroelectric semiconductors for solar energy conversion applications,” *Chem. Mater.* **32**, 9542–9550 (2020).
- ¹⁶K. N. Heinselman, L. S. Roberts, J. L. Young, and A. Zakutayev, “Reduced synthesis temperatures of SrNbO₂N perovskite films for photoelectrochemical fuel production,” *J. Mater. Res.* **37**, 424–435 (2022).
- ¹⁷K. R. Talley, R. White, N. Wunder, M. Eash, M. Schwarting, D. Evenson, J. D. Perkins, W. Tumas, K. Munch, C. Phillips, and A. Zakutayev, “Research data infrastructure for high-throughput experimental materials science,” *Patterns* **2**, 100373 (2021).
- ¹⁸N. Britun and J. Hnilica, “Optical spectroscopy for sputtering process characterization,” *J. Appl. Phys.* **127**, 211101 (2020).
- ¹⁹U. Fantz, “Basics of plasma spectroscopy,” *Plasma Sources Sci. Technol.* **15**, S137–S147 (2006).
- ²⁰F. Clénet, P. Braud, and G. Turban, “Experimental study of an RF magnetron discharge for thin-film deposition,” *Surf. Coat. Technol.* **97**, 528–532 (1997).
- ²¹J. Shin and J. Mazumder, “Composition monitoring using plasma diagnostics during direct metal deposition (DMD) process,” *Opt. Laser Technol.* **106**, 40–46 (2018).
- ²²S.-K. Wu and K.-H. Tseng, “Composition control of R.F.-sputtered Ni₂MnGa thin films using optical emission spectroscopy,” *Mater. Trans.* **43**, 871–875 (2002).
- ²³L. Rachdi and M. Hofmann, “Use of optical emission spectroscopy to predict silicon nitride layer properties,” *Vacuum* **191**, 110322 (2021).
- ²⁴A. Salimian, A. Aminishahavarani, and H. Upadhyaya, “Artificial neural networks to predict sheet resistance of indium-doped zinc oxide thin films deposited via plasma deposition,” *Coatings* **12**, 225 (2022).
- ²⁵Y.-P. Yang, T.-Y. Lu, H.-H. Lo, W.-L. Chen, P. J. Wang, W. Lai, Y.-K. Fuh, and T. T. Li, “Machine learning assisted classification of aluminum nitride thin film stress via in-situ optical emission spectroscopy data,” *Materials* **14**, 4445 (2021).
- ²⁶D. Drury, K. Yazawa, A. Mis, K. Talley, A. Zakutayev, and G. L. Brennecke, “Understanding reproducibility of sputter-deposited metastable ferroelectric wurtzite Al_{0.6}Sc_{0.4}N films using in situ optical emission spectrometry,” *Phys. Status Solidi RRL* **15**, 2100043 (2021).
- ²⁷J. Posada, M. Jubault, A. Bousquet, E. Tomasella, and D. Lincot, “In-situ optical emission spectroscopy for a better control of hybrid sputtering/evaporation process for the deposition of Cu(In,Ga)Se₂ layers,” *Thin Solid Films* **582**, 279–283 (2015).
- ²⁸Z. Weiss, “Emission yields and the standard model in glow discharge optical emission spectroscopy: Links to the underlying physics and analytical interpretation of the experimental data,” *Spectrochim. Acta, Part B* **61**, 121–133 (2006).
- ²⁹Z. Weiss, “Calibration methods in glow discharge optical emission spectroscopy: A tutorial review,” *J. Anal. At. Spectrom.* **30**, 1038–1049 (2015).
- ³⁰H.-H. Ley, “Analytical methods in plasma diagnostic by optical emission spectroscopy: A tutorial review,” *J. Sci. Technol.* **6**, 49–66 (2014).
- ³¹Z. Weiss, P. Ashcheulov, N. Lambert, A. Taylor, J. Lorincik, K.-d. Sung, M. Davydova, and V. Mortet, “Analysis of boron- and phosphorus-doped diamond layers by glow discharge optical emission spectroscopy in argon and neon,” *Vacuum* **210**, 111890 (2023).
- ³²T. Head, M. Kumar, H. Nahrstaedt, G. Louppe, and I. Shcherbatyi (2022), “Scikit-optimize/scikit-optimize,” Zenodo.
- ³³Y. K. Wakabayashi, Y. Krockenberger, T. Otsuka, H. Sawada, Y. Taniyasu, and H. Yamamoto, “Intrinsic physics in magnetic Weyl semimetal SrRuO₃ films addressed by machine-learning-assisted molecular beam epitaxy,” *Jpn. J. Appl. Phys.* **62**, SA0801 (2023).
- ³⁴B. Shahriari, K. Swersky, Z. Wang, R. P. Adams, and N. de Freitas, “Taking the human out of the loop: A review of Bayesian optimization,” *Proc. IEEE* **104**, 148–175 (2016).